UC Irvine

UC Irvine Previously Published Works

Title

Mapping of Heterogeneous Catalyst Degradation in Polymer Electrolyte Fuel Cells

Permalink

https://escholarship.org/uc/item/5k76v320

Journal

Advanced Energy Materials, 10(28)

ISSN

1614-6832

Authors

Cheng, Lei

Khedekar, Kaustubh

Talarposhti, Morteza Rezaei

et al.

Publication Date

2020-07-01

DOI

10.1002/aenm.202000623

Peer reviewed

Mapping of Heterogeneous Catalyst Degradation in Polymer Electrolyte Fuel Cells

Lei Cheng, *Kaustubh Khedekar, Morteza Rezaei Talarposhti, Andrea Perego, Michael Metzger, Saravanan Kuppan, Sarah Stewart, Plamen Atanassov, Nobumichi Tamura, Nathan Craig, Iryna V. Zenyuk* and Christina M. Johnston**

Dr. Lei Cheng, Dr. Michael Metzger, Dr. Saravanan Kuppan, Dr. Sarah Stewart, Dr. Nathan Craig, Dr. Christina M. Johnston
Bosch Research and Technology Center North America, Sunnyvale, CA 94085, USA
E-mail: lei.cheng2@us.bosch.com, christina.johnston@us.bosch.com

Kaustubh Khedekar, Prof. Plamen Atanassov, Prof. Iryna V. Zenyuk
Department of Material Science and Engineering, University of California Irvine, Irvine, CA 92697, USA
E-mail: iryna.zenyuk@uci.edu

Morteza Rezaei Talarposhti, Dr. Andrea Perego, Prof. Plamen Atanassov, Prof. Iryna V. Zenyuk
Department of Chemical and Bimolecular Engineering; National Fuel Cell Research Center
University of California, Irvine, CA 92697, USA

Dr. Nobumichi Tamura
Advanced Light Source, Lawrence Berkeley National Laboratory, Berkeley CA 94720, USA

Abstract

Pt catalyst in polymer electrolyte fuel cells degrades heterogeneously as the catalyst particles are exposed to local variations throughout the catalyst layer during operation. State-of-the-art analytical techniques for studying degradation of Pt catalyst do not possess fine spatial resolution to elucidate such non-uniform degradation behavior at a large electrode level. A new methodology is developped to spatially resolve and quantify the heterogeneous Pt catalyst degradation over a large area (several cm^2) of aged MEAs based on synchrotron X-ray micro-diffraction. PEFC single cells are aged using voltage cycling as an accelerated stress test and the degradation heterogeneity at a micrometer length scale is visualized by mapping Pt catalyst particle size after voltage cycling. We demonstrated in details that the Pt catalyst particle size growth is non-uniform and follows the flow field geometry. The Pt particle size growth is greater in the area under the flow field land, while it is minimal in the area under the flow field channel. Additional non-uniformity is observed with the Pt particle size increasing more rapidly at the gas outlet area of than the Pt particle size at the inlet area.

1. Introduction

Platinum (Pt) catalyst durability in polymer electrolyte fuel cells (PEFCs) has been a grand technical challenge, hindering the large-scale use of PEFCs, particularly for vehicle application Significant efforts have been spent to better understand the fundamental mechanisms and mitigation strategies for degradation.[1–4] Generally, Pt catalyst degradation results in the change in the number of accessible catalytic active site for the electrochemical reaction, which is commonly characterized by the loss of electrochemical surface area (ECSA) in laboratory evaluations[5]. The reduced ECSA is assigned principally to (a) loss of catalytically active surface area resulting from Pt catalyst nanoparticle size growth by Pt dissolution and redeposition; (b) loss of active catalyst loading by Pt dissolution and subsequent precipitation in the membrane or near the cathode/membrane interface, forming disconnected Pt band (c) loss of accessible active catalyst resulted from carbon support corrosion. Mechanism (a) of Pt particle growth is considered to be a significant contribution, with some reports assigning it to 30-50 % ECSA loss in half cell measurement in accelerated stress tests (AST)[6]. Similarly, a full cell MEA AST protocol involves load cycling in range of 0.60 V- 0.95 V (or 1.00 V), conditions at which Pt oxidation and re-deposition occurs as major degradation, leading to Pt catalyst particle size growth without apparent carbon support corrosion[1,7,8]. Transmission electron microscopy (TEM) and X-ray diffraction (XRD) are commonly used for post-mortem analysis and show Pt particle size growth in very localized area and averaged Pt particle size over relatively larger areas, respectively [9,10].

Practically, in both small scale single cell MEA evaluation or large scale PEFC stack operation, catalyst coated membranes (CCMs) are sandwiched between cathode/anode gas

3

diffusion layers (GDLs). And the entire five-layer assembly is placed between bipolar plates (BPPs), where the BPP land sections press down the GDL under compression to maintain good electrical contact and gases flow mainly in the channels of the BPP. Depending on the flow field geometry and fluid dynamics at specific operation conditions, there may exist local variations in mass transport, heat transport, water transport and current distribution over the area of the catalyst layer, where local water accumulation, strongly influenced by the flow field geometry, plays an important role affecting catalyst durability[11–13]. Pt catalyst particles at specific locations are exposed to different local conditions (e.g. relative humidity (RH), liquid water content and gas composition (H_2 and O_2 gradients in the case of H_2/air operation), thus the localized degradation behavior likely deviates[12–15]. So far, 1-D segmented cell design has shown some progress in delivering insights into electrocatalyst degradation from start-up and shut-down cycles, showing non-uniform ECSA loss between inlet and outlet regions[16,17]. But current understanding of this heterogeneity is still limited due to experimental limitation in resolving local degradation[1,18–22]. Particularly, how the heterogeneity of catalyst degradation quantitatively correlates to its specific location remains unknown. Thus, there is a need for detailed analytics of the Pt catalyst degradation with a fine 2-D spatial resolution to elucidate such non-uniform Pt degradation behavior at the electrode level. In this letter, we report a new methodology to spatially resolve and quantify Pt catalyst particle degradation over a large area (several cm^2) of aged MEAs.

2. Results and Discussion

The performance degradation of the aged MEA after the load cycling AST is clearly visible in the IR corrected polarization curves, Figure 1 (a). At current density of 1 A/cm^2, the potential after 30,000 AST cycles is 98 mV less than the beginning of life (BOL). The voltage loss at a

geometric current density of 50 mA/cm^2 as a function of the logarithm of normalized ECSA is plotted in Figure 1 (b). A slope of 75 mV/decade is observed at 80ºC, which agrees well the 70 mV/decade formulated by Zihrul *et al.* [23], indicating the observed voltage loss is almost entirely due to the oxygen reduction reaction (ORR) kinetics. In our voltage cycling AST between 0.60 V and open circuit potential (OCV, approximately 0.94 V), the major electro-catalyst degradation mechanisms are expected to be Pt oxidation and reduction/dissolution and redisposition. Carbon-support corrosion is expected to be less severe at these conditions compared to those at high potentials above 1.2 V[24,25]. The loss of ECSA was observed to be 70% after voltage cycling, expected to be mostly due to Pt nano-particle size growth. This is supported by scanning electron microscope (SEM) /energy dispersive X-ray spectroscopy (EDS) observation shown in Figure 1 (c) and (d). We observed neither Pt band formation within the reinforced Nafion XL membrane nor microstructure change/thinning of catalyst layer (due to carbon support corrosion) for the entire 1 cm length cross-section. Statistics of catalyst layer thickness measurements and additional details can be found in supplementary information (SI) Table S1.

Figure 2. shows the 2-D mapping of Pt particle size distribution in three different areas (1 cm × 1 cm)   of a 25 cm^2 sized MEA,using synchrotron X-ray micro-diffraction[26]. The locations are near the gas inlet, near the gas outlet and in the middle of the serpentine flow field. The corresponding flow field pattern for the 1cm^2 area is shown in the inset (upper right corner) for each map in Figure 2. The detailed location on the MEA respective to the entire 25 cm^2 and whole flow field pattern is shown in Figure S1. The spot size of the X-ray beam was 2 μm × 5 μm. A 1 cm^2 area was mapped in 200 μm and 500 μm step increments along the x and y axis, respectively, as shown in Figure 2. At every data point of each map, a diffraction ring pattern was collected (shown in Figure S2). The Pt diffraction rings were integrated to get

peak intensity vs two theta for the Pt diffraction peak width determination. The particle size of Pt was estimated using the Sherrer equation from the corrected peak width (for details concerning the X-ray diffraction instrumental broadening correction see SI). In the 2-D particle size mapping, distinct Pt particle growth was observed in the area under the flow field land and under the flow field channel. In the control MEA without AST, particle size is mostly uniformly distributed over the entire 1 cm^2 area in all the three mapped locations. In comparison, after AST in air/H_2 at 100% RH conditions, the degradation of Pt catalyst particles was no longer uniform. We observed that Pt catalyst particle-size growth followed the triple channel serpentine pattern of flow field: under the channel area, the particle size growth is minimum, but the Pt particles under the land area experienced significant particle growth. For example, in Figure 1 (f), the estimated average particle size under the channel is close to 3.7 nm, similar to the values in the control shown in Figure 1 (c). Under the land, the particle size is about 5-6 nm. Same trend is also observed in both locations close to the outlet and at the middle of the serpentine channel. Note that the outlet area sees most severe particle growth where land area shows particle size as large as 6-7 nm.

For quantitative comparison of particle size distributions, the estimated particle sizes of each mapped 1 cm^2 area are plotted in histogram as shown in Figure 3. For the MEA not aged in the voltage cycling AST protocol, the corresponding histogram shows a Gaussian like symmetric peak with relatively narrower distribution of particle sizes, indicative of one mono-dispersed particle size for each location. Close to the inlet area, the peak position was around 3.1 nm. We use this value as an indicator of average particle size for comparison. This average particle size agrees with previous reported values of 2.9 and 3.0 nm measured by localized TEM methods [27,28], also similar to the 3.3 nm estimated by XRD[29] for the same TKK TEC10E50E catalyst. It is worth noting here that the particle size distribution is

generated from 1000 measurements for each 1 cm^2 area, which statistically presents significantly more Pt particles and a different length-scale than histogram derived from several localized TEM micrograph or averaged XRD estimation. It may contribute to the difference of Pt particle size distribution observed in previous reports[5,9,30]. For this same non-aged MEA, at the areas close to the outlet and in the middle of the flow field, it showed single particle size distribution with an average particle sizes both around 3.7 nm, slightly larger than in the inlet area. This gentle particle size growth might be due to the multi-voltage break-in procedure[31]. As a result of the Pt catalyst degradation induced during the AST of 30,000 voltage cycles, the particle size distribution was dramatically altered. Firstly, the particle size distribution in all three locations evolved into bimodal distributions, drastic contrast to the unimodal particle size distribution observed in the non-aged MEA. Two apparent peaks were observed at 3.7 nm and 4.9 nm at the inlet area of the post-AST MEA, the lower value corresponding to particle sizes in the area under flow-field channel and higher values corresponding to those under the flow-field land area. Similar bimodal distribution was also observed at the area in the middle of the flow field. For the area close to the gas outlet, it was observed that particle size under the channel and land both further increased having a low value of ~ 4.7 nm for channel and high value of ~ 6.0 nm for land. Additionally, it is also inferable from the peak height in the histogram that the fraction of the large particles increases from the inlet area to the outlet areas, suggesting more severe particle growth near the gas outlet than the gas inlet. Such phenomenon that Pt catalyst particle size grows more near the outlet has also been observed in start-up and shut down (SUSD) cycles using TEM[32].

The Pt catalyst nanoparticle size distribution along x-axis (the direction across several channel-land-channel) is further visualized in Figure 4. For the mapped area of post-AST

7

MEA, the Pt particle size distribution follows a periodicity with a peak to peak distance of ~ 1.8 mm, matching with the periodicity of channel-land pattern of the graphite BPP flow field. (The BPP flow field has a channel to channel distance of 1.71 mm, with a channel width of 0.79 mm and land width of 0.92 mm). In comparison, the Pt catalyst particle size is uniformly distributed along the x-axis in the non-aged MEA control. The observed differences/dependence in Pt catalyst nanoparticle growth under the land/channel geometry are likely attributable to the difference of water accumulated in the catalyst layer under the land area and channel area. Generally, liquid water accumulates and is trapped under the land[33–36], particularly at 100% RH. The greater accumulation of liquid water under the land is generally attributable to the lower temperature. The water accumulation generally occurs inside the GDL, which may further increase the local liquid water contetn near and in the subsequent catalyst layer. Locally, the increased presence of liquid water is expected to result in an increase in the effective mobility of dissolved Pt species and thus an acceleration in the local Pt particle size growth during AST voltage cycling[37]. For the channel area, the rate of Pt particle size growth is expected to be less prominent due to lower effective Pt species mobility at lower water content[38].

After 30,000 voltage cycles between 0.6 V and OCV, the voltage of the aged MEA is 506 mV at 1 A/cm^2 current density, 98 mV lower than the pristine MEA, corresponding to a 16.7% power loss. The ECSA loss observed in the aged sample was 70% as determined electrochemically by hydrogen underpotential deposition (H$_{upd}$) charge. The performance loss mainly attributed to catalyst particle size growth as no Pt band formation and apparent damage of catalyst layer support structure or thinning were observed. The catalyst degradation under the channel areas was small as Pt particle size remained approximately 3.7 nm , whereas average Pt particle sizes almost doubled under the land area, indicating more severe

degradation, as shown in Figure 5 a. Pt particle surface area estimated by particle size derived from micro-diffraction was 50% more than the ECSA values determined by the H_{upd} methods. This is consistent with the analysis by Ferreira *et al.*[10] considering none-spherical Pt particle, less Pt surface area in contact with carbon support and Pt particle agglomeration. The degradation of electrocatalyst under the land area likely contributes a significant portion to the total performance loss, which also results in performance disproportion between channel area and land area. A 2-D MEA performance model implemented in COMSOL was used to qualitatively assess the local operation conditions at the catalyst layer interfacing GDL under the flow field channel and land areas at 0.6 V in air/H_2 environment condition[39]. The locally observed Pt catalyst particle growth (Figure 5 a) was compared with the local conditions (oxygen mole fraction, temperature, Δ gas pressure and current densities) at the surface of the catalyst layer interfacing GDL in Figure 5 b-e. The model suggests higher O_2 gas mole fraction and higher current densities at the cathode catalyst area under the flow field channel area. The temperature and pressure differences were small. Their impact on the local degradation rate of catalyst is possibly overwhelmed by the impact from water accumulation. According to the simulation, the relative electrical power output from the channel area is higher than from the land area at the beginning of life when the catalyst particle size is uniformly distributed in the catalyst layer. This power output disparity increases further as a result of the experimentally observed preferential catalyst degradation under the flow field land area, implying that the electro-catalysts in channel areas is the major contributor to performance/power output in an aged cell, more so in severely aged MEA. In our aging experiments, a 32% power loss is estimated in the catalyst layer under land area (54% of total electrode area), which corresponds to the total 16.7% power loss of the entire MEA, with an assumption of nearly no performance loss in the channel area as Pt nano-particle size did not change in observation.

9

3. Conclusion

In summary, we spatially resolved the PEFC Pt catalyst degradation of a voltage cycled MEA between 0.6 V and OCV in air/H_2 environment by mapping Pt particle size using synchrotron x-ray micro-diffraction with micrometers resolution. It is found that Pt electro-catalyst particle size growth and degradation is non-uniform and follows the flow field channel/land pattern. After voltage cycling, Pt particle size growth was larger in the area under the flow-field land than prior to cycling, while the particle size growth in the area under the flow-field channel was similar to prior to cycling. A similar disparity was observed in areas close to the gas inlet, gas outlet and in the middle of the flow field across the entire 25 cm^2 area, with significantly more severe Pt particle growth observed at the outlet area than the inlet area. 2-D modelling suggests that the local cell performance difference between land and channel areas diverges even more after aging. The methodology can be adopted to study any large sized MEA (lab scale or commercial size) catalyst degradation under various aging conditions or flow field designs, providing a valuable and unique tool for studying fuel cell MEA catalyst aging and flow field design. The finding in this study emphasizes the strong impact of flow field geometry on the local degradation behavior of the electro-catalyst, providing new insights to the design and engineering of PEFC for prolonged fuel cell performance retention and durability.

4. Experimental Section

Pt/C based MEAs were purchased from Ion Power Inc., Denmark, with an active area of 25cm^2 and loading of 0.3 mg$_{Pt}$cm^{-2} on both cathode and anode side. The Pt/C catalyst is

TEC10E50E supplied by Tenaka Kikinzoku Kogyo. These MEAs contained Nafion XL membrane of thickness 27.5μm with a PTFE rich reinforcement layer in the membrane.

The MEAs were tested in fuel cell fixture from Scribner Associates with POCO graphite triple-serpentine flow field consisted of 30 equally spaced channels with square bottom (0.92 mm land width, 0.79 mm channel width and 1 mm channel depth, see Figure S1.). Sigracet 29 BC, a non-woven carbon paper with 5 wt% PTFE treatment and hydrophobic microporous layer (MPL) with a total thickness of 235μm was used as gas diffusion layers on both electrodes (GDL). To achieve an optimal GDL compression of 22%, PTFE coated fiberglass along with virgin PTFE gaskets were used with the thicknesses of 150 μm and 27.5 μm respectively. The fixture was assembled at a torque of 13.5 Nm. Accelerated stress tests (AST) and polarization curve measurements were all performed using the 850e Fuel Cell Test Stand with maximum current load of 100 A from Scribner Associates, Connecticut, USA. The AST were performed using a square wave potential profile from 0.60V to open circuit potential (OCV) with 3 seconds holds at each potential for 30,000 cycles at 80 °C. Cyclic voltammograms (CV), linear sweep voltammograms (LSV) and electrochemical impedance spectroscopy (EIS) were measured using VSP-BioLogic potentiostat (potential resolution of 5μV and maximum current of 4A) for ECSA, H_2 cross-over and cell electrical resistance. Cyclic voltammetry measurements were carried out from 0.095 V to 0.8 V at a scan rate of 20 mVs^{-1}. LSVs were measured from 0.05 V to 0.8 V at a scan rate of 1 mVs^{-1}. EIS was done from 10 kHz to 0.01 Hz at zero bias vs OCV.

All the aforementioned tests were performed in H_2/N_2 environment with 200 sccm/300 sccm flow rates at 100% relative humidity (RH) at atmospheric pressure. Polarization curves were generated by holding the cell at constant currents for 3 minutes and measuring the corresponding voltage values with multiple points. Voltage values were averaged over these 3 minutes for both forward and backward scans. The test was performed at 150 kPa(a) backpressure with a stoichiometry of 1.5/1.8 in H_2/air environment (anode/cathode) in 100% RH conditions. The procedure was preceded with a recovery protocol to retrieve all the recoverable losses and ensure test is performed at the same conditions. The beginning of life (BOL) stage was achieved by performing a voltage break-in procedure on a fresh MEA which consisted of potential holds of 30 seconds at 0.80 V, 0.60 V and 0.30 V respectively until constant current was achieved[31].

An epoxy mounting/cutting method was used to prepare cross-section for scanning electron microscope (SEM) and energy dispersive spectroscopy (EDS) characterization. An area of about 1 cm × 1 cm in the middle of the MEA was first cut from the MEA, and then was sandwiched between stainless steel and glass plate to keep flat. The assembly was mounted in epoxy and then sectioned to expose the cross-section. The cross-section was further polished using multiple polishing paper with finish progressively increasing from 320 grit to 1200 grit. The polished cross-section was imaged in a JOEL-7200F field emission scanning electron microscope, equipped with an Oxford Instruments X-Max^N EDS detector. Catalyst layer thickness measurement was carried out using ImageJ. Multiple measurements were taken at various locations across the entire 1 cm length of the cross-section.

The synchrotron X-ray micro-diffraction mapping/imaging measurements were conducted at Beamline 12.3.2 of the Advanced Light Source (ALS) at Lawrence Berkeley National Laboratory. A monochromatic X-ray beam (10 keV) was focused to ∼2×5 μm^2 by a pair of Kirkpatrick−Baez mirrors. The sample was mounted on a high-resolution x−y scan stage and tilted 25° relative to the incident X-ray beam. 2D X-ray diffraction images were recorded in reflection mode with a two-dimensional Pilatus-1 M detector mounted at 60° to the incoming X-ray, approximately 150 mm from the probe spot. Exposure time at each position was 10 s. The detector has a pixel size of 0.17 mm. Calibrations for distance, center channel position, and tilt of detector were performed on the basis of a powder pattern obtained from a reference Al_2O_3 powder taken at the same geometry than the samples. For mapping/imaging of each 1×1 cm^2 area of each MEA samples. A 2-D scan of 50 × 20 points was performed with a step size of 200 μm on x-axis and 500 μm on y-axis. Finer 200 μm step size in x-axis was adopted to resolve the flow field channel (~0.78 mm) and land (~0.92 mm). The X-ray scan diffraction data was then processed by XMAS[40]. Debye-Scherrer rings were integrated along the azimuthal direction and the resulting peak width were determined by fitting of a 2d Lorentzian function with an angular resolution of∼0.02°. Instrumental broadening were estimated using large Al_2O_3 crystals powder in the exact same detector configuration.

A 2-D, steady-state, continuum, PEMFC performance model from literature was used to simulate the different conditions under the land and channel present during the experiments [39]. The equations were implemented and solved using the commercial package COMSOL Multiphysics. The model includes seven spatial layers within the MEA: anode GDL, anode MPL, anode CL, membrane, cathode CL, cathode MPL, cathode GDL, as well as anode

channel, anode land, cathode channel, and cathode land. The model simulates coupled heat

transfer, mass transfer, chemical reaction, and phase change.

References

[1]   R. Borup, J. Meyers, B. Pivovar, Y. S. Kim, R. Mukundan, N. Garland, D. Myers, M. Wilson, F. Garzon, D. Wood, P. Zelenay, K. More, K. Stroh, T. Zawodzinski, J. Boncella, J. E. McGrath, M. Inaba, K. Miyatake, M. Hori, K. Ota, Z. Ogumi, S. Miyata, A. Nishikata, Z. Siroma, Y. Uchimoto, K. Yasuda, K. I. Kimijima, N. Iwashita, *Chem. Rev.* **2007**, *107*, 3904.

[2]   X. X. Wang, M. T. Swihart, G. Wu, *Nat. Catal.* **2019**, *2*, 578.

[3]   A. Kneer, N. Wagner, *J. Electrochem. Soc.* **2019**, *166*, F120.

[4]   M. Uchimura, S. Sugawara, Y. Suzuki, J. Zhang, S. S. Kocha, *ECS Trans.* **2008**, *16*, 225.

[5]   C. A. Rice, P. Urchaga, A. O. Pistono, B. W. McFerrin, B. T. McComb, J. Hu, *J. Electrochem. Soc.* **2015**, *162*, F1175.

[6]   R. Sharma, S. M. Andersen, *ACS Catal.* **2018**, *8*, 3424.

[7]   A. Ohma, K. Shinohara, A. Iiyama, T. Yoshida, A. Daimaru, *ECS Trans.* **2011**, *41*, 775.

[8]   X. Z. Yuan, H. Li, S. Zhang, J. Martin, H. Wang, *J. Power Sources* **2011**, *196*, 9107.

[9]   R. L. Borup, J. R. Davey, F. H. Garzon, D. L. Wood, M. A. Inbody, *J. Power Sources* **2006**, *163*, 76.

[10]   P. J. Ferreira, G. J. La O', Y. Shao-Horn, D. Morgan, R. Makharia, S. Kocha, H. A. Gasteiger, *J. Electrochem. Soc.* **2005**, *152*, 2256.

[11]   U. N. Shrivastava, K. Tajiri, *J. Electrochem. Soc.* **2016**, *163*, F107.

[12]   L. Dubau, L. Castanheira, F. Maillard, M. Chatenet, O. Lottin, G. Maranzana, J. Dillet, A. Lamibrac, J.-C. Perrin, E. Moukheiber, A. ElKaddouri, G. De Moor, C. Bas, L.

Flandin, N. Caqué, *Wiley Interdiscip. Rev. Energy Environ.* **2014**, *3*, 540.

[13]   Y. Chatillon, C. Bonnet, F. Lapicque, *Fuel Cells* **2014**, *14*, 581.

[14]   Y. Li, K. Moriyama, W. Gu, S. Arisetty, C. Y. Wang, *J. Electrochem. Soc.* **2015**, *162*, F834.

[15]   Y. Li, C. Y. Wang, *J. Electrochem. Soc.* **2017**, *164*, F171.

[16]   S. Komini Babu, D. Spernjak, J. Dillet, A. Lamibrac, G. Maranzana, S. Didierjean, O. Lottin, R. L. Borup, R. Mukundan, *Appl. Energy* **2019**, *254*, 113659.

[17]   J. Durst, A. Lamibrac, F. Charlot, J. Dillet, L. F. Castanheira, G. Maranzana, L. Dubau, F. Maillard, M. Chatenet, O. Lottin, *Appl. Catal. B Environ.* **2013**, *138–139*, 416.

[18]   J. A. Gilbert, N. N. Kariuki, X. Wang, A. J. Kropf, K. Yu, D. J. Groom, P. J. Ferreira, D. Morgan, D. J. Myers, *Electrochim. Acta* **2015**, *173*, 223.

[19]   J. A. Gilbert, A. J. Kropf, N. N. Kariuki, S. DeCrane, X. Wang, S. Rasouli, K. Yu, P. J. Ferreira, D. Morgan, D. J. Myers, *J. Electrochem. Soc.* **2015**, *162*, F1487.

[20]   M. M. Mench, N. T. Vezirogulu, E. Gaglan Kumbar, Eds. , *Polymer Electrolyte Fuel Cell Degradation*, Elsevier Science, **2011**.

[21]   J. C. Meier, C. Galeano, I. Katsounaros, A. A. Topalov, A. Kostka, F. Schüth, K. J. J. Mayrhofer, *ACS Catal.* **2012**, *2*, 832.

[22]   G. S. Harzer, J. N. Schwämmlein, A. M. Damjanović, S. Ghosh, H. A. Gasteiger, *J. Electrochem. Soc.* **2018**, *165*, F3118.

[23]   P. Zihrul, I. Hartung, S. Kirsch, G. Huebner, F. Hasché, H. A. Gasteiger, *J. Electrochem. Soc.* **2016**, *163*, F492.

[24]   T. Mittermeier, A. Weiß, F. Hasché, H. A. Gasteiger, *J. Electrochem. Soc.* **2018**, *165*, F1349.

[25]   T. Mittermeier, A. Weiß, F. Hasché, G. Hübner, H. A. Gasteiger, *J. Electrochem. Soc.*

2017, *164*, F127.

[26]   M. Kunz, N. Tamura, K. Chen, A. A. MacDowell, R. S. Celestre, M. M. Church, S. Fakra, E. E. Domning, J. M. Glossinger, J. L. Kirschman, G. Y. Morrison, D. W. Plate, B. V Smith, T. Warwick, V. V Yashchuk, H. A. Padmore, E. Ustundag, *Rev. Sci. Instrum.* **2009**, *80*, 35108.

[27]   E. Pizzutilo, S. Geiger, J. P. Grote, A. Mingers, K. J. J. Mayrhofer, M. Arenz, S. Cherevko, *J. Electrochem. Soc.* **2016**, *163*, F1510.

[28]   O. J. Curnick, B. G. Pollet, P. M. Mendes, *RSC Adv.* **2012**, *2*, 8368.

[29]   V. A. Sethuraman, J. W. Weidner, A. T. Haug, M. Pemberton, L. V. Protsailo, *Electrochim. Acta* **2009**, *54*, 5571.

[30]   G. S. Harzer, A. Orfanidi, H. El-Sayed, P. Madkikar, H. A. Gasteiger, *J. Electrochem. Soc.* **2018**, *165*, F770.

[31]   I. V. Zenyuk, R. Taspinar, A. R. Kalidindi, E. C. Kumbur, S. Litster, *J. Electrochem. Soc.* **2014**, *161*, F3091.

[32]   Y. Yamashita, S. Itami, J. Takano, M. Kodama, K. Kakinuma, M. Hara, M. Watanabe, M. Uchida, *J. Electrochem. Soc.* **2016**, *163*, F644.

[33]   A. Z. Weber, R. L. Borup, R. M. Darling, P. K. Das, T. J. Dursch, W. Gu, D. Harvey, A. Kusoglu, S. Litster, M. M. Mench, R. Mukundan, J. P. Owejan, J. G. Pharoah, M. Secanell, I. V. Zenyuk, *J. Electrochem. Soc.* **2014**, *161*, F1254.

[34]   A. Turhan, S. Kim, M. Hatzell, M. M. Mench, *Electrochim. Acta* **2010**, *55*, 2734.

[35]   M. C. Hatzell, A. Turhan, S. Kim, D. S. Hussey, D. L. Jacobson, M. M. Mench, *J. Electrochem. Soc.* **2011**, *158*, 32.

[36]   S. Kim, M. M. Mench, *J. Electrochem. Soc.* **2009**, *156*, B353.

[37]   W. Bi, Q. Sun, Y. Deng, T. F. Fuller, *Electrochim. Acta* **2009**, *54*, 1826.

[38]   C. Takei, K. Kakinuma, K. Kawashima, K. Tashiro, M. Watanabe, M. Uchida, *J. Power Sources* **2016**, *324*, 729.

[39]   L. M. Pant, M. R. Gerhardt, N. Macauley, R. Mukundan, R. L. Borup, A. Z. Weber, *Electrochim. Acta* **2019**, *326*, 134963.

[40]   N. Tamura, in *Strain Dislocation Gradients from Diffr.* (Eds.: R. Barabash;, G. Ice), IMPERIAL COLLEGE PRESS, **2014**, pp. 125–155.

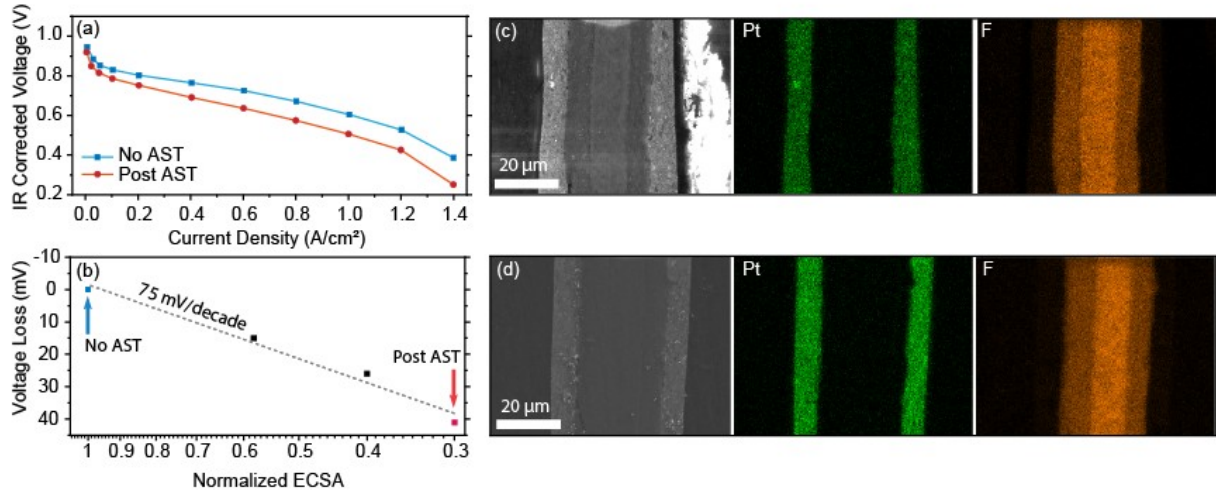Figure 1. (a) IR corrected polarization curves of the MEA measured BOL and post AST; (b) Voltage

difference between post AST and BOL at geometric current density of 50 mA/cm^2; (c) SEM images,

Pt and F EDS maps of no AST MEA; (d) SEM images, Pt and F EDS maps of post AST MEA

(cathode side is on the right)
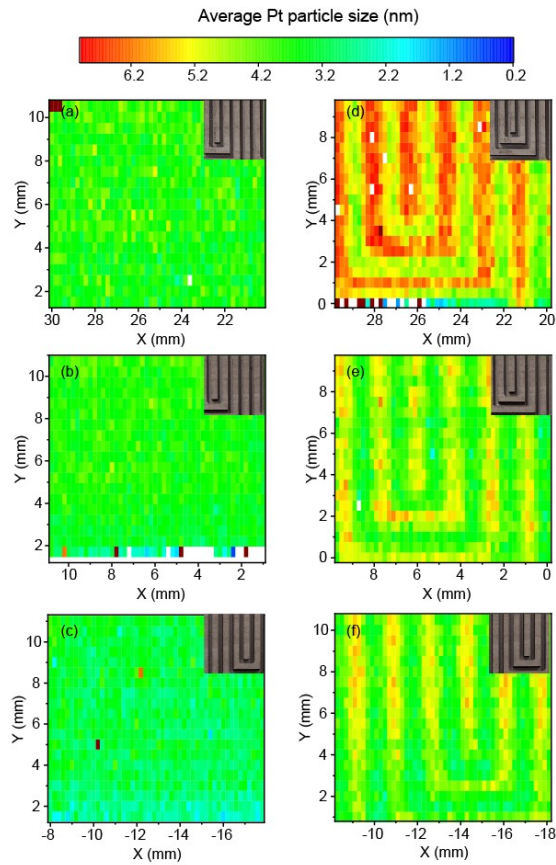
Figure 2. Pt catalyst nano-particle size mapping of 1 cm × 1 cm area (a) near gas outlet of the non-aged MEA (b) in the middle of the flow field of the non-aged MEA (c) near gas inlet of the non-aged MEA (d) near gas outlet of the post-AST MEA (e) in the middle of the flow field of the post-AST MEA (f) near gas inlet of the post-AST MEA. Insets show the corresponding flow field geometry for each measured 1 cm by 1 cm location.
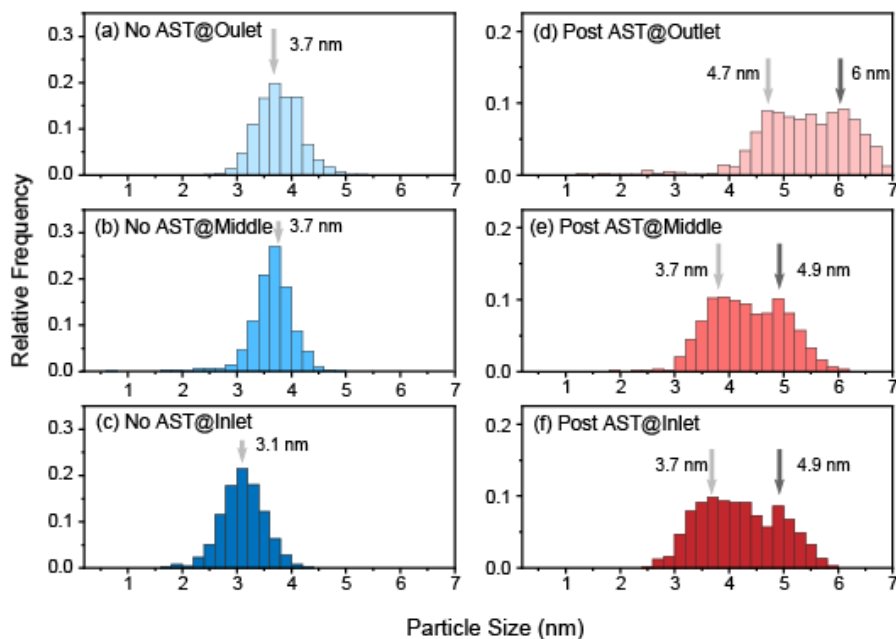
Figure 3. Pt catalyst particle size distribution in MEA that did not undergo AST at the outlet (a), middle (b) and inlet (c) location. Pt catalyst particle size distribution for MEA post AST at outlet (d), middle (e), and inlet (f) location
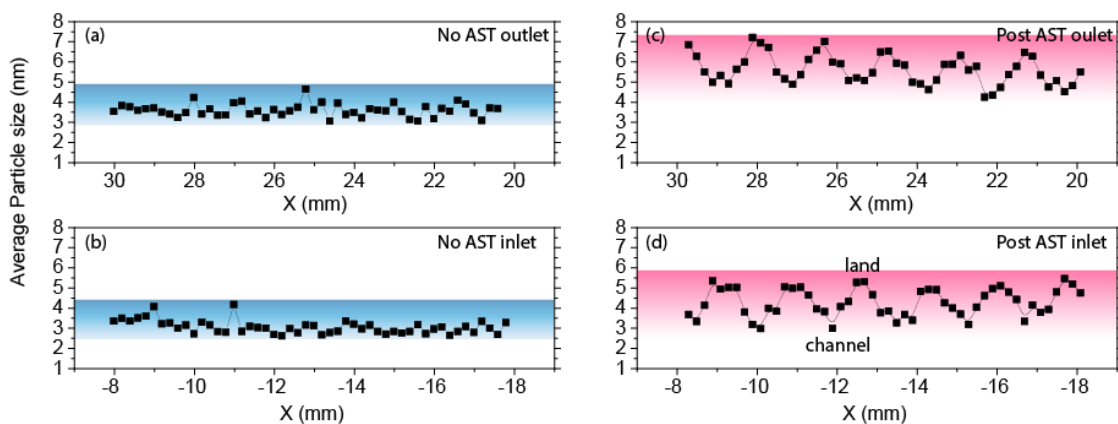

Figure 4. Pt catalyst nanoparticle size distribution along x-axis in MEA that did not undergo AST at the outlet (a) and inlet (b) location. Pt catalyst nanoparticle size distribution along x-axis in MEA post AST at outlet (c) and inlet (d) location.
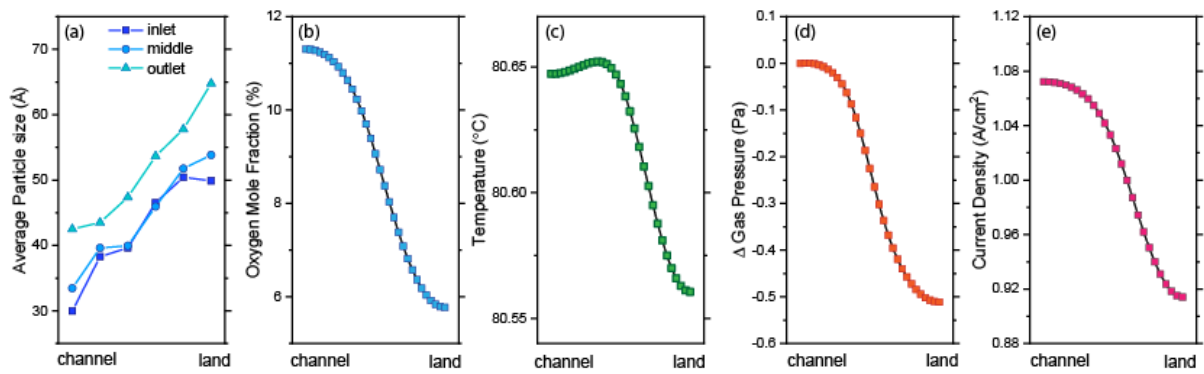
Figure 5. 1-D distribution of (a) Pt catalyst nanoparticle size after AST and simulated (b) oxygen mole fraction (c) catalyst surface temperature (d) gas pressure difference and (e) current density from the center of one channel to the center of neighboring land.

Synchrotron X-ray micro-diffraction mapping is adopted to visualize the heterogeneity of catalyst degradation in polymer electrolyte fuel cell (PEFC). The map show the degradation hetergeniety follows the flow field geometry with catalyst particle degrading faster under the land area. This provides a unique tool to study PEFC catalyst degradation, delivering new insights into design and engineering of durable PEFC.

Fuel Cells

Lei Cheng[*], *Kaustubh Khedekar, Morteza Rezaei Talarposhti, Andrea Perego, Michael Metzger, Saravanan Kuppan, Sarah Stewart, Plamen Atanassov, Nobumichi Tamura, Nathan Craig, Iryna V. Zenyuk*[*]*and Christina M. Johnston*[*]

Mapping of Heterogeneous Catalyst Degradation in Polymer Electrolyte Fuel Cells
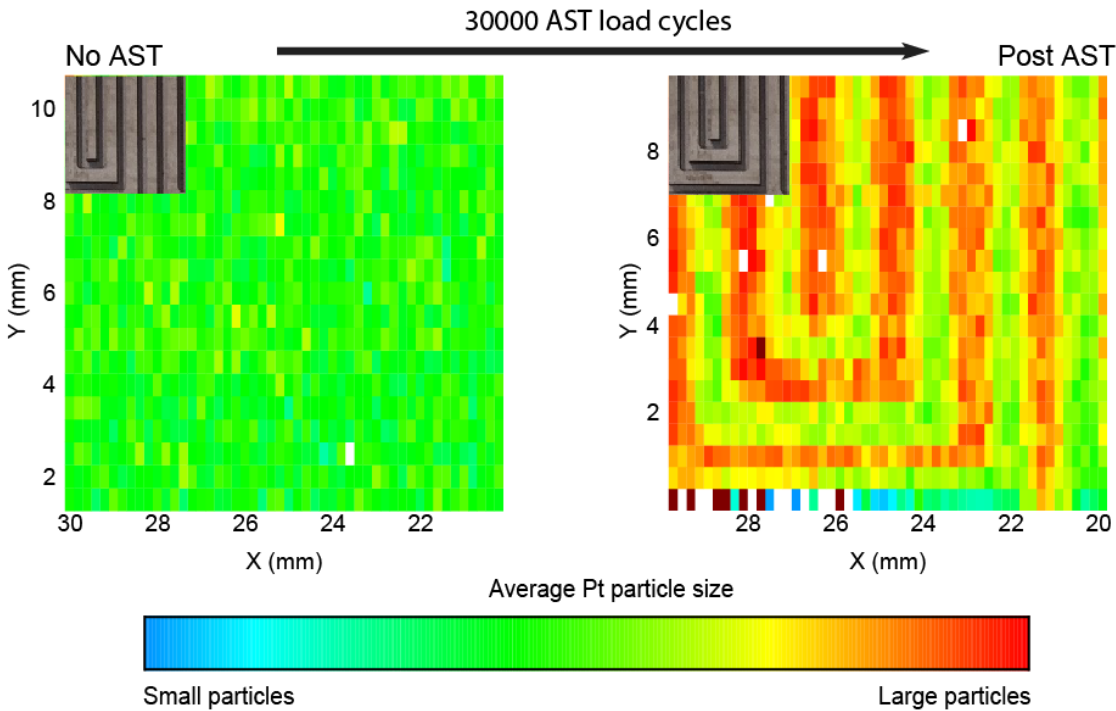
ToC figure

Supporting Information

Mapping of Heterogeneous Catalyst Degradation in Polymer Electrolyte Fuel Cells

Lei Cheng[*], *Kaustubh Khedekar, Morteza Rezaei Talarposhti, Andrea Perego, Michael Metzger, Saravanan Kuppan, Sarah Stewart, Plamen Atanassov, Nobumichi Tamura, Nathan Craig, Iryna V. Zenyuk*[*]*and Christina M. Johnston*[*]
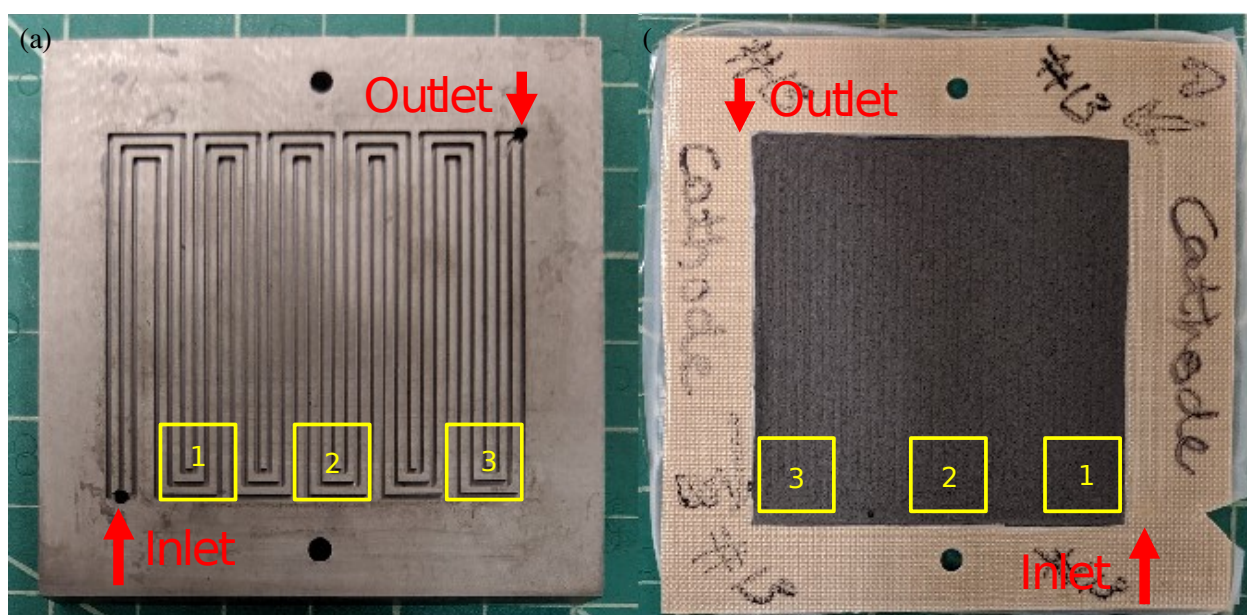

Figure S1. (a) Cathode side graphite bipolar plate with 3-serpentine flow field design; (b) Post-AST MEA with GDL and sub-gasket on viewed from the cathode side. Yellow box indicated the corresponding area being mapped. Note the flow field pattern is mirrored to the imprints of GDL on the cathode side.

Figure S2 (a) is a typical diffraction image. In Figure S2 (b) Pt (red) diffraction ring were indexed with and graphite (yellow) diffraction ring labelled. As shown in the diffraction image, these Pt rings were broad and low in intensity, corresponding to broad peak and thus crystalline/grain sizes. The (220) Pt diffraction rings were integrated and plotted in intensity vs two theta in Figure S2 (c). Eight Pt (220) diffraction peaks (using 10 keV monochromatic X-ray) were shown from different locations of the mapped MEA. The peak width were calculated by fitting the diffraction peak to a lorentzian peak. Instrumental correction was done by subtracting peak width Al_2O_3 reference crystal peak width from the measured peak width.
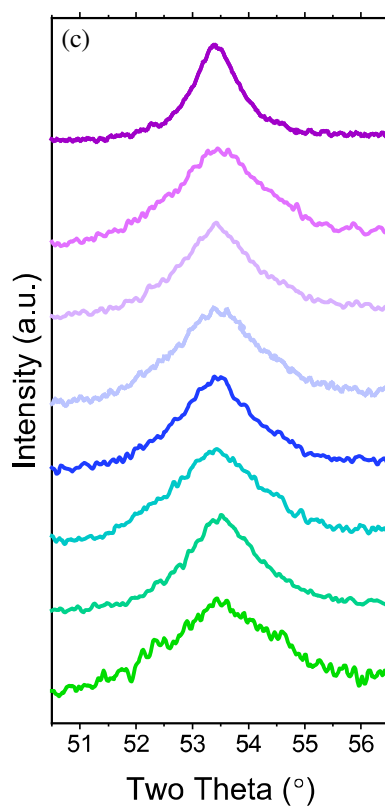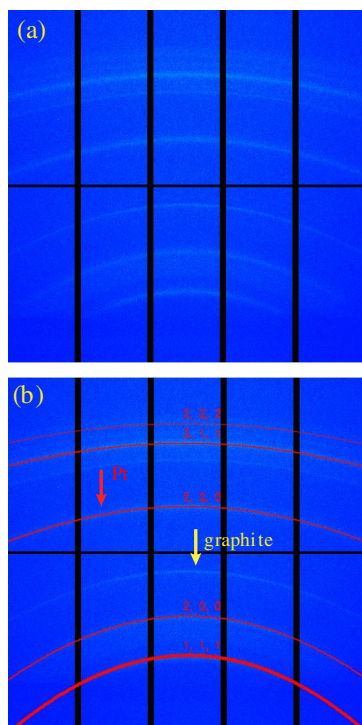
Figure S2. (a) a micro-diffraction image; (b) indexed micro-diffraction pattern with Pt peaks (red color); (c) examples of (220) Pt diffraction peaks integrated from diffraction ring patterns at several different locations of the MEA

Location #	Catalyst Layer Thickness (μm)			
	No AST anode	No AST cathode	Post AST anode	Post AST cathode
1	8.1	7.3	7.0	7.9
2	9.6	8.7	8.1	8.4
3	9.2	8.4	9.5	9.1
4	7.9	8.2	9.3	8.7
5	8.0	7.4	8.9	8.6
6	9.3	9.9	8.7	9.1
7	7.5	7.9	8.0	7.4
8	7.0	6.1	7.9	7.8
9	10.1	9.8	7.9	7.6
10	8.3	7.8	7.7	8.1
11	8.9	8.5	8.1	8.6
12	9.2	8.7	8.3	8.0
Average	**8.6**	**8.2**	**8.3**	**8.3**
STD	0.9	1.0	0.7	0.5

Table S1. Anode and cathode catalyst layer thickness across the entire 1 cm the cross-section